



Mostaquimur Rahman, A. S. M., Rosolem, R., Kollet, S. J., & Wagener, T. (2019). Towards a computationally efficient free-surface groundwater flow boundary condition for large-scale hydrological modelling. *Advances in Water Resources*, 123, 225-233.

<https://doi.org/10.1016/j.advwatres.2018.11.015>

Peer reviewed version

License (if available):
CC BY-NC-ND

Link to published version (if available):
[10.1016/j.advwatres.2018.11.015](https://doi.org/10.1016/j.advwatres.2018.11.015)

[Link to publication record in Explore Bristol Research](#)
PDF-document

This is the author accepted manuscript (AAM). The final published version (version of record) is available online via Elsevier at <https://www.sciencedirect.com/science/article/pii/S0309170818303701> . Please refer to any applicable terms of use of the publisher.

University of Bristol - Explore Bristol Research

General rights

This document is made available in accordance with publisher policies. Please cite only the published version using the reference above. Full terms of use are available:
<http://www.bristol.ac.uk/pure/about/ebr-terms>

1 **Towards a computationally efficient free-surface groundwater flow**
2 **boundary condition for large-scale hydrological modelling**

3 M. Rahman¹, R. Rosolem^{1,2}, S. J. Kollet^{3,4}, and T. Wagener^{1,2}

4 ¹Department of Civil Engineering, University of Bristol, UK

5 ²Cabot Institute, University of Bristol, UK

6 ³IBG-3, Research Centre Jülich, Germany

7 ⁴Center for High-Performance Scientific Computing in Terrestrial Systems, Geoverbund
8 ABC/J, Germany

9

10 **Abstract**

11 Shallow groundwater is a critical component of the terrestrial water cycle. It sustains
12 baseflow in rivers, supplies root zones with soil moisture during dry periods, and directly
13 influences the land-atmosphere exchange processes. Nonetheless, the integration of
14 groundwater into large-scale hydrological models remains challenging. The most detailed
15 way of representing groundwater dynamics is to incorporate three-dimensional, variably
16 saturated flow processes in the subsurface representation of hydrological models. However,
17 such detailed modelling is still a challenge for global hydrological applications, mainly due to
18 its high computational demand. In this study, a free-surface boundary condition called the
19 Groundwater Flow Boundary (GFB) is developed to represent groundwater dynamics in a
20 more computationally-efficient manner than the full three-dimensional models do. We
21 evaluate GFB using two synthetic test cases, namely an infiltration experiment and a tilted-v
22 catchment, which focus on groundwater recharge and discharge processes, respectively. The
23 simulation results from GFB are compared with a three-dimensional groundwater flow model
24 and with an over-simplified approach using a free-drainage lower boundary condition to
25 assess the impact of our assumptions on model results. We demonstrate that GFB is

26 computationally more efficient compared to the three-dimensional model with limited loss in
27 model performance when simulating infiltration and runoff dynamics.

28 **1. Introduction**

29 The dynamics of shallow groundwater table affect the variability of soil moisture and
30 evapotranspiration at the land surface [*Chen and Hu, 2004; Kollet and Maxwell, 2008; Lam et*
31 *al., 2011; Soyly et al., 2011*]. Spatial variability of groundwater table depth (WTD) creates
32 lateral groundwater flow, which sustains baseflow in rivers [e.g., *Miller et al., 2016*]. Due to
33 its importance, recent studies have strongly suggested that groundwater dynamics should not
34 be ignored in large-scale hydrological modelling [*Clark et al., 2015*].

35 Numerical modelling has long been a key approach to study the hydrological cycle given that
36 observations only provide an incomplete picture [*Fan et al., 2013*]. Contemporary
37 hydrological models that focus on the terrestrial component of the water cycle can broadly be
38 classified into three groups: catchment-scale hydrological models, global hydrological
39 models, and land surface models [*Archfield et al., 2015*]. At the catchment-scale, models that
40 integrate both surface and groundwater fluxes in a spatially explicit manner have been
41 utilized for a while [e.g., *Abbott et al., 1986; Qu and Duffy, 2007; Smerdon et al., 2007;*
42 *Kollet and Maxwell, 2008; Shen and Phanikumar, 2010; Rahman et al., 2014*]. These models
43 can represent heterogeneity in the subsurface and simulate groundwater flow at high spatial
44 and temporal resolutions. Their application has largely focused on understanding the detailed
45 interactions of hydrologic processes over smaller domains (i.e., from catchments to river
46 basins).

47 In contrast, global hydrological models operate (so far mainly) at relatively coarse spatial
48 resolutions (order of 10 to 100 km) and often focus on streamflow simulations at continental
49 to global scales [*Wood et al., 1997; Arnell, 1999; Döll et al., 2003*]. Classically, these models

50 generally considered a simplified representation of subsurface hydrology, either neglecting or
51 strongly over-simplifying groundwater dynamics. In recent years, some global hydrological
52 models have started to consider groundwater dynamics more explicitly [e.g., *de Graaf et al.*,
53 2015; *Sutanudjaja et al.*, 2018]. It has also been advocated that global models should capture
54 the effects of heterogeneity in topography, soils, and vegetation on hydrological cycle better
55 by operating at a higher spatial resolution (1 km) [*Wood et al.*, 2011; *Archfield et al.*, 2015;
56 *Bierkens et al.*, 2015].

57 A comprehensive method of considering groundwater dynamics is to incorporate an
58 integrated hydrological model into the global models. In recent years, it has been
59 demonstrated that fully integrated hydrological models can be applied at a continental scale
60 [*Keune et al.*, 2016; *Maxwell and Condon*, 2016]. However, due to its numerical complexity,
61 such a modelling practice generally demands substantial computational resources, which
62 limits our ability for more detailed analyses of uncertainties and consequently the impacts of
63 underlying assumptions [*Beven and Cloke*, 2012; *Kelleher et al.*, 2017].

64 Several previous studies have proposed simplified parameterizations for groundwater
65 dynamics to overcome the issue of computational burden while modelling the integrated
66 surface-groundwater system at large (e.g., continental to global) scales. For instance, the land
67 surface models were originally developed to simulate the exchange of water and energy
68 between the land surface and atmosphere [*Pitman*, 2003]. Due to the importance of shallow
69 groundwater dynamics on land surface processes, the land surface modelling community has
70 proposed simplified parametrizations to simulate groundwater dynamics over large domains
71 [*Yeh and Eltahir*, 2005a; *Niu et al.*, 2011; *Zeng et al.*, 2016; *Oleson et al.*, 2013]. These
72 simplified methods consider either probability distributions of soil, vegetation, and
73 topography across the model domain to incorporate the subgrid-scale variability of WTD

74 [e.g., *Yeh and Eltahir*, 2005b], or use an implicit representation of groundwater flow [e.g.,
75 *Famiglietti and Wood*, 1994; *Koster et al.*, 2000]. Nevertheless, to our knowledge, none of
76 these approaches has been tested against the results from a fully integrated three-dimensional
77 hydrological model using synthetic studies to evaluate the impact of assumptions inherent in
78 these different parameterizations. We believe this is an important and currently missing step
79 in model development, which would allow modellers to better identify advantages and
80 quantify limitations in the theoretical development of any approach prior to its
81 implementation in complex modelling frameworks [*Clark et al.*, 2015].

82 In this study, we introduce a new explicit and computationally-efficient approach for
83 representing groundwater flow processes, namely the Groundwater Flow Boundary (GFB).
84 Because of its computational efficiency, the GFB approach can potentially be applied to
85 simulate groundwater dynamics over large domains in global hydrological and land surface
86 modelling applications at high spatial and temporal resolutions. We present simulation
87 examples in comparison with the three-dimensional hydrological model ParFlow [*Ashby and*
88 *Falgout*, 1996; *Kollet and Maxwell*, 2006; *Maxwell*, 2013] to evaluate the proposed GFB
89 approach, including the impact of our assumptions.

90 **2. Theory of the Groundwater Flow Boundary (GFB) condition**

91 A detailed, physics-based subsurface representation generally solves Richards' equation
92 [*Richards*, 1931] on a three-dimensional grid (Figure 1a), where the mathematical problem is
93 closed via appropriate initial and boundary conditions. In contrast, Figure 1b illustrates the
94 free-drainage (FD) lower boundary condition approach below one-dimensional isolated
95 shallow soil columns neglecting groundwater, which has been adopted by many large-scale
96 models and later modified using simple groundwater storage and water table
97 parameterizations [*Bierkens*, 2015]. Figure 1c shows a schematic of the proposed modelling

98 framework in this study. In this approach, the vertical model domain is divided into a shallow
 99 soil column (discretized in several model grids) and a deep aquifer. In the shallow soil
 100 column, Richards' equation simulates the variably saturated flow of water in three spatial
 101 dimensions.

$$102 \quad S_s S_w \frac{\partial \psi_s}{\partial t} + \varphi \frac{\partial S_w(\psi_s)}{\partial t} = \nabla \cdot \mathbf{q} + q_s \quad (1)$$

$$103 \quad \mathbf{q} = -K_s K_r \nabla(\psi_s - z)$$

104 where S_s is specific storage coefficient [L^{-1}], S_w is relative saturation [-], φ is porosity [-], ψ_s is
 105 subsurface pressure head [L], t is time [T], \mathbf{q} is water flux [LT^{-1}], q_s is the source/sink term
 106 [LT^{-1}] (e.g., infiltration from precipitation or evaporation), K_s is saturated hydraulic
 107 conductivity [LT^{-1}], K_r is relative permeability [-], and z is the depth below surface [L]. In
 108 this equation, the negative z axis points downward starting at the land surface. The van
 109 Genuchten relationships [*van Genuchten*, 1980] are used to describe the relative saturation
 110 and permeability functions in Equation 1. The Neumann type boundary condition for
 111 Richards' equation can be written as

$$112 \quad K_s K_r \nabla(\psi_s - z) = q_b \quad (2)$$

113 where q_b is the flux at the boundary [LT^{-1}].

114 In two spatial dimensions, the equation of transient groundwater flow in an unconfined
 115 aquifer can be written as [*Pinder and Bredehoeft*, 1968; *Prickett and Lonquist*, 1971;
 116 *Meenal and Eldho*, 2011]

$$117 \quad S_y \frac{\partial h}{\partial t} = \nabla(\mathbf{T}_r \nabla h) + q_r \quad (3)$$

$$118 \quad h = \frac{\Delta z_a}{2} + \psi_a \quad (4)$$

119 where S_y is specific yield [-], h is the depth integrated hydraulic head in the aquifer [L], \mathbf{T}_r is
 120 the transmissivity of the aquifer [L^2T^{-1}], q_r is recharge/discharge rate [LT^{-1}], Δz_a is aquifer
 121 thickness [L], and ψ_a is the pressure head in aquifer [L]. Note that \mathbf{T}_r is calculated by
 122 integrating K_s over h . This approach assumes that the variation of the saturated depth (Δh) is
 123 negligible compared to its absolute value (i.e., $\Delta h \ll h$).

124 Assuming pressure and flux continuity at the interface between the aquifer and the overlying
 125 soil layer (Figure 1c)

$$126 \quad \psi_s = \psi_a = \psi \quad (5)$$

$$127 \quad q_b = q_r \quad (6)$$

128 Note that such assumption of pressure and flux continuity was proposed by *Kollet and*
 129 *Maxwell* [2006] to integrate subsurface and surface water flow. Equation 3 can be solved for
 130 q_r as follows

$$131 \quad q_r = S_y \frac{\partial h}{\partial t} - \nabla(\mathbf{T}_r \nabla h) \quad (7)$$

132 Substituting q_r in equation (2) for q_b at the interface results in

$$133 \quad -K_s K_r \nabla(\psi - z) = S_y \frac{\partial h}{\partial t} - \nabla(\mathbf{T}_r \nabla h) \quad (8)$$

134 Thus, the groundwater flow equation is introduced as the lower boundary condition of
 135 Richards' equation for the soil columns.

136 In the proposed approach, groundwater dynamics are simulated (Equation 3) in two spatial
 137 dimensions using a single model layer (Figure 1c), which is computationally more efficient
 138 than a full 3D model resolving also vertical flow components in the aquifer. In the theoretical
 139 development of the GFB, we apply two major assumptions: (1) the negligible variability of

140 saturated depth compared to its absolute value (i.e., $\Delta h \ll h$); and, (2) the linear interpolation
141 of the pressure between the aquifer and overlying soil layer.

142 **3. Methods**

143 In this study, we use the three-dimensional hydrological model ParFlow. We implement GFB
144 in ParFlow, which allows us to compare the proposed approach with a detailed 3D model of
145 groundwater flow. The ParFlow model along with the GFB implementation and the setup of
146 the numerical experiments are described below.

147 **3.1. The physics-based hydrological model ParFlow**

148 ParFlow solves Richards' equation in three spatial dimensions considering a cell-centred
149 finite-difference/finite control volume approximation in space and an implicit backward Euler
150 scheme in time. The subsurface-surface flow coupling is achieved by applying a free-surface
151 overland flow boundary condition at the land surface [Kollet and Maxwell, 2006]. In this
152 approach, the kinematic wave equation is solved at the interface between the land surface and
153 subsurface considering pressure and flux continuity. Honouring the topographic slopes in an
154 approximate fashion, a terrain following grid is implemented in ParFlow [Maxwell, 2013].

155 We consider three configurations of ParFlow to evaluate our proposed free-surface boundary
156 condition that represents groundwater dynamics in this study (i.e., the GFB). The standard
157 formulation (FULL hereafter) includes variably saturated groundwater flow from the bottom
158 of the aquifer to the land surface in three spatial dimensions. The GFB configuration
159 incorporates our proposed groundwater flow boundary condition (Section 2) in ParFlow
160 approximating the aquifer in two spatial dimensions. In contrast, the FD configuration
161 mimics the classical description of water flow through soil still available in many LSMs by
162 implementing a free drainage boundary condition in ParFlow assuming water flow through
163 the soil columns only along the vertical direction.

164 3.2. Setup of the numerical experiments

165 We evaluate our proposed modelling approach using two synthetic test cases, namely the
166 infiltration and the tilted-v catchment experiments (similar to *Kollet et al., 2017*). The
167 infiltration experiment compares the variably saturated flow through subsurface after a
168 precipitation event to assess the capability of the different model configurations (i.e., FULL,
169 GFB, and FD) to simulate recharge. The tilted-v catchment experiment compares the
170 discharge simulated by the three model configurations. The setup of the two experiments is
171 described below.

172 3.2.1. Infiltration experiment

173 Figure 2a shows the model setup of the infiltration experiment. A model domain of 2,500 m²
174 is discretized using a uniform lateral grid resolution ($\Delta x = \Delta y$) of 10 m, yielding 5 grid cells
175 in both x and y dimensions in all three (i.e., FULL, GFB, and FD) model configurations. In
176 the FULL configuration, a total subsurface depth of 100 m (motivated by the global pattern of
177 WTD presented in *Fan et al. [2013]*) is divided into 2,000 layers considering a uniform
178 vertical resolution of $\Delta z = 5$ cm. The lower boundary condition is assumed to be no-flow. The
179 FD configuration considers only 10 m deep soil columns (similar to soil domains typically
180 observed in land surface models) that are divided into 200 vertical layers approximating a
181 uniform $\Delta z = 5$ cm. As mentioned in the previous section, a free-drainage boundary condition
182 is applied at the bottom of the soil columns in FD. The GFB configuration also considers
183 shallow soil columns extending 10 m downward starting at the land surface. The soil columns
184 in GFB are divided into 200 vertical layers assuming a uniform $\Delta z = 5$ cm. Unlike the FD
185 setup, a 90-m deep aquifer is included underneath the shallow soil columns in GFB. The
186 shallow soil columns and the aquifer are integrated using the free-surface boundary condition
187 at the interface as discussed in Section 2.

188 The simulation period considered in the infiltration experiment is 5 days, with a constant time
189 step of $\Delta t = 15$ min. A spatially uniform rainfall rate of 5 mmh^{-1} is applied over the model
190 domain for the first 10 hrs of the simulation period. The infiltration experiment is performed
191 for 12 soil textural classes (Table 1) [e.g., *Rawls et al.*, 1982; *Saxton and Rawls*, 2006;
192 *Ghanbarian-Alavijeh et al.*, 2010] and the results of the three model configurations (FULL,
193 GFB, FD) are compared. All soil types are prescribed in a spatially uniform manner.

194 3.2.2. Tilted-v catchment

195 The experimental setup of the tilted-v catchment is illustrated in Figure 2b. The model
196 domain considered in this experiment is 2.1×1.0 km that is slanted in the x and y -directions.
197 A 100 m wide channel is located in the centre of this slanted model domain with the outlet
198 located at $y=0$. The tilted-v catchment is discretized using 21 and 10 grid cells in x and y -
199 direction, respectively ($\Delta x = \Delta y = 100$ m). The total subsurface depth is 100 m in FULL,
200 which is divided into 200 equal vertical grids considering $\Delta z = 50$ cm. In this configuration, a
201 no-flow boundary condition is prescribed at the bottom of the model domain (i.e., 100 m
202 below surface). The GFB configuration, in contrast, considers a 90-m thick aquifer that is
203 overlain by soil columns extending 10 m below surface. A uniform vertical grid spacing of
204 $\Delta z = 50$ cm is used to divide the 10-m soil columns of GFB into 20 model layers. Identical to
205 the infiltration experiment, these soil columns are coupled to the aquifer using our proposed
206 free-surface boundary condition (i.e., the GFB) at the interface. A simulation period of 20 h is
207 considered for this experiment with a constant $\Delta t = 15$ min. Groundwater table (WT) is
208 initially located at the land surface and no rainfall is applied in this experiment. Notice that
209 the FD experiment does not solve for lateral flow, hence there is no expected contribution to
210 discharge in the tilted-v catchment experiment. For this reason, the FD configuration is
211 excluded from this experiment. As with the infiltration experiment, all soil types are
212 uniformly prescribed in the tilted-v experiment.

213 **4. Results and discussion**

214 **4.1. Infiltration experiment**

215 The goal of this experiment is to assess how the wetting front from a specific rainfall event
216 develops and further interacts with a pre-defined water table within the domain for all three
217 model configurations. Figure 3 compares relative soil moisture (S_w) profiles (0-2.5 m below
218 land surface) from infiltration experiment simulated by the three model configurations, i.e.,
219 FULL, GFB, and FD for a silty soil. Note that only the S_w profiles from the central cell of the
220 model domain (Figure 2) are presented here.

221 In all three configurations, the relatively shallow soil layers are initially dry because the
222 groundwater table is located at 1.5 m below the land surface. Infiltration starts immediately
223 with the onset of the precipitation in all three cases, which is observed by the increased
224 saturation level of the soil layers starting at the top of the profiles. After about 5 h, the
225 infiltration front reaches the groundwater table (WT) in FULL. The shallow S_w simulated by
226 this configuration gradually decreases as the infiltration front moves deeper once the
227 precipitation ceases.

228 The movement of the infiltration front in GFB generally agrees well with that of the FULL
229 configuration. Figure 3b shows that the rise and recession of the WT due to the precipitation
230 event is captured by GFB. Though, it appears that groundwater recharge simulated by GFB is
231 smaller compared to the FULL configuration. During the recession, the shallow soil layers
232 dry out faster in GFB. The S_w profile simulated by FD, on the other hand, dries out
233 considerably faster compared to both FULL and GFB. While the WT was initially located at
234 1.5 m below surface in all three configurations, it quickly moves deeper in FD due to the
235 persistent gravity drainage imposed by the lower boundary condition, which is intuitive.

236 Both GFB and FD show differences in simulated soil moisture compared to FULL (Figure 3).
 237 We quantify these differences in S_w profiles using Mean Difference (MD), which is
 238 calculated as

$$239 \quad MD = \frac{1}{nt} \frac{1}{nd} \sum_{i=1}^{i=nt} \sum_{j=1}^{j=nd} (a_{i,j} - b_{i,j}) \quad (9)$$

240 where MD is the mean difference between the soil moisture profiles a and b, t is the time
 241 instance, and d denotes soil layer. Note that only the soil columns up to 10 m below surface
 242 from the three model configurations are considered in the calculation of MD. This analysis
 243 reveals that MD is 0.0081 for GFB, while the FD configuration shows an MD = 0.0909
 244 (Figure 3). GFB, therefore, performs substantially better than FD in reproducing the S_w
 245 profile simulated by the FULL configuration for silty soil.

246 The numerical experiment described in Figure 3 gives us some initial insight into the
 247 performance of our newly proposed approach in comparison with the FULL and FD
 248 configurations, respectively. We further expand this experiment by evaluating the
 249 performance of GFB against FULL and FD for 12 soil textural classes (Table 1) following
 250 the same initialization procedure described for the silty soil simulations in Figure 3. Figure 4
 251 shows the MD of S_w profiles simulated by GFB and FD compared to that of FULL for 12
 252 soils. The best performance of GFB is observed for clay soil with an MD of 10^{-4} . The largest
 253 difference between the S_w profiles from the two configurations is observed for sand, which is
 254 indicated by the largest MD = 0.034. Such model behaviour is observed due to the linear
 255 interpolation of pressure between the aquifer and lowermost soil layer, which is a key
 256 assumption in the formulation of GFB. For a fine-textured soil (e.g., clay) the saturation-
 257 pressure head relationship is linear in the van Genuchten relationship [e.g., *Assouline et al.*,
 258 1998]. However, a coarse-textured soil (e.g., sand) shows non-linear behaviour, which
 259 weakens our assumption of a linear pressure profile between the lowest soil layer and aquifer.

260 For the FD configuration, the MD also increases for relatively coarse-textured soils, which is
261 consistent with GFB. However, differences are systematically larger for FD in comparison to
262 the differences observed in GFB for all soil types. In general, FD substantially underestimates
263 S_w compared to FULL (MD > 0) due to the prescribed free-drainage lower boundary
264 condition. The best model performance is again observed for clay soil with an MD = 0.0124.
265 In contrast, sand shows an MD = 0.4937, indicating differences between the S_w profiles
266 simulated by FULL and FD. Therefore, Figure 4 indicates that GFB performs considerably
267 better than FD in reproducing FULL simulated S_w for all soil classes.

268 The results discussed in Figures 3 and 4 focused on understanding the sensitivity of the
269 dynamic differences in soil wetness from the three configurations for various soil classes.
270 Another important aspect of our model development is to test how these configurations
271 behave under different initial WTD conditions. Figure 5 shows the MD between the S_w
272 profiles from the FULL and GFB configurations for 12 soil types (Table 1) considering a
273 number of initial depths of WT. The result demonstrates that for an initial WTD > 20 m, the
274 S_w profiles from FULL and GFB are identical for all soil types. For WTD \leq 20m, the
275 discrepancies between the two configurations increase from fine to coarse-textured soils due
276 to the assumption of a linear pressure profile between the lowest soil layer and aquifer. The
277 differences between the S_w profiles for clay at all initial WT are negligible. The loam soil
278 shows higher MD compared to clay, which reaches its maximum (MD = 0.014) for an initial
279 WT located at 10 m below land surface. For sand, the highest MD = 0.068 is observed when
280 WT is initially located at 7 m below the land surface. Therefore, for fine-textured soils (e.g.,
281 clay), the S_w profiles from FULL and GFB generally agree well. However, in coarse-textured
282 soils (e.g., sand), differences between the FULL and GFB configurations are relatively high
283 for $0.25 \text{ m} \leq \text{WTD} \leq 20 \text{ m}$.

284 It has been discussed earlier that the FULL and GFB configurations consider 2000 (up to 100
285 m below surface) and 200 (up to 10 m below surface) vertical model layers, respectively in
286 the infiltration experiment. Because of this difference in vertical model layers, the total
287 computing time required (t_{cpu}) by the two configurations to perform this experiment will vary.
288 Figure 6 shows the t_{cpu} of FULL and GFB for different soil textures presented in Table 1 with
289 initial WT located at 1.5 m below surface. This plot clearly shows that the t_{cpu} of GFB is
290 considerably lower than that of FULL for all soil types. This is also substantiated by the mean
291 t_{cpu} of 272 s and 42 s over all the soil types for the FULL and GFB configurations,
292 respectively. In summary, Figure 6 demonstrates that the t_{cpu} of GFB is about 6 times lower
293 than that of FULL, which indicates that the former is computationally much more efficient.

294 **4.2. Tilted-v catchment**

295 The previous section evaluated GFB considering a test case focusing on infiltration. In this
296 section, we test the capability of the GFB approach to simulate discharge due to lateral
297 groundwater flow in a tilted-v catchment. Figure 7 shows cumulative discharge at the outlet
298 of the tilted-v catchment (Figure 2b) from FULL and GFB. Note that the soil hydraulic
299 properties of loam soil (Table 1) is considered in these simulations. Along the x - and y - axis,
300 topographic slopes (SL) of $SL_x = 0.005$ and $SL_y = 0.002$ (Figure 2b) are prescribed in this
301 numerical experiment. The WT is located at the land surface initially ($WTD = 0$) in both
302 configurations. Figure 7 shows that GFB marginally underestimates the discharge simulated
303 by FULL. Despite this underestimation, good overall agreement between the discharge
304 simulated by FULL and GFB is observed (i.e., low MD of $0.002 \text{ m}^3\text{s}^{-1}$ between the discharge
305 time series simulated by the two configurations).

306 The required CPU time (t_{cpu}) to simulate the tilted-v experiment by the FULL and GFB
307 configurations are 35 s and 8 s, respectively. As discussed in section 3.2.2, the FULL

308 configuration considers 200 vertical model grid cells for the tilted-v catchment. In contrast,
309 the GFB configuration consists 20 grid cells below surface, which is the reason of
310 discrepancies between the t_{cpu} from the two configurations. This difference in t_{cpu} shows that
311 GFB is computationally more efficient than FULL in simulating the tilted-v catchment,
312 which is consistent with the results from the infiltration experiment.

313 Figure 8 shows the flow depth along the x -axis of the tilted-v catchment at $y = 500$ m (see
314 Figure 2) at different simulation times. This figure shows low flow depth close to the lateral
315 boundaries (i.e., $x = 0$ and $x = 2100$ m), which increases gradually towards the central
316 channel. The maximum flow depth is observed at the channel of the catchment. At $t = 1$ h,
317 GFB underestimates flow depth compared to the FULL configuration. This underestimation
318 of flow depth is consistent with the lower discharge simulated by GFB observed in Figure 7.
319 At $t = 5$ h and 10 h, the GFB performs well in reproducing the flow depth simulated by
320 FULL. In contrast, slight overestimation of the flow depth by GFB is observed at $t = 15$ h.
321 The spatial variability of the flow depth observed in Figure 8 occurs due the effect of
322 topographic slopes that forces groundwater to converge at the central channel of the
323 catchment. This figure demonstrates that the overall variability of flow depth along the
324 topographic slopes simulated by FULL is reproduced well by the GFB configuration.

325 We now assess the impact of soil types on the differences between discharge simulated by
326 FULL and GFB. Figure 9 compares the differences between FULL and GFB simulated
327 cumulative discharge at the outlet of tilted-v catchment considering three different soil types,
328 i.e., sand, loam, and clay (coarse, medium, and fine-textured, respectively). Note $SL_x = 0.005$
329 and an initial WTD = 0 is considered in this experiment, which is identical to that of Figure 8.
330 The smallest difference between FULL and GFB is observed for clay soil in Figure 9. For
331 sand, on the other hand, the largest difference between FULL and GFB simulated cumulative
332 discharge is noted. The MD between FULL and GFB simulated discharge for clay, loam, and

333 sand are 9×10^{-7} , 0.0018, and $0.0420 \text{ m}^3\text{s}^{-1}$, respectively. This analysis shows that the
334 differences between runoff from the two configurations increase from fine to coarse-textured
335 soils, which is consistent with the infiltration experiment.

336 As a final test, we investigate the sensitivity of runoff from GFB due to different topographic
337 slopes along the x-axis (SL_x) of the tilted-v catchment considering the same initialization
338 steps in Figure 8. Figure 10a plots the MD between runoff from the GFB and FULL
339 configurations as a function of SL_x . In general, the runoff from GFB compares well with that
340 of FULL for all SL_x , which is indicated by the low MD values (on the order of 10^{-3} to 10^{-2}
341 m^3s^{-1}). Figure 10a demonstrates that differences between FULL and GFB simulated discharge
342 generally increase from mild to steep SL_x . For $SL_x \leq 0.01$, GFB underestimates ($\text{MD} > 0$)
343 runoff compared to FULL. For higher SL_x values, in contrast, overestimation ($\text{MD} < 0$) of
344 runoff by GFB is observed.

345 Figure 10b presents the t_{cpu} from the FULL and GFB configurations to simulate tilted-v
346 experiment as a function of topographic slope (SL_x). This figure depicts that the t_{cpu} required
347 by GFB is very low compared to that of FULL. The t_{cpu} of FULL increases from mild to steep
348 SL_x . The minimum (35 s) and maximum (794 s) t_{cpu} of FULL are observed for $SL_x = 0.005$
349 and 0.25, respectively. In contrast to FULL, the maximum t_{cpu} required by GFB is 8 s, which
350 is observed for $SL_x = 0.25$. The mean t_{cpu} values over all slopes are 322 s and 7 s, respectively
351 for FULL and GFB. H Therefore, our proposed approach is about 43 times faster than the
352 FULL configuration.

353 In this study, we have presented an efficient approach of representing groundwater dynamics
354 in large-scale numerical models by reducing the number of computational nodes in the
355 vertical direction. It is important to note that previous studies have also proposed an
356 “effective hillslope” concept that adopts a pseudo 2-D approach to reduce the computational

357 demand of simulating the lateral groundwater flow in hydrological models [*Troch et al.*,
358 2003; *Hazenberg et al.*, 2015]. This concept can be applied in conjunction with our proposed
359 GFB to further enhance the computational efficiency of the large scale hydrological models.

360 **5. Summary and conclusions**

361 We have proposed a novel free-surface Groundwater Flow Boundary (GFB) condition to
362 parameterize groundwater dynamics in land surface or large-scale hydrological models that
363 require representation of groundwater dynamics in an efficient manner. In our approach, the
364 groundwater flow in an unconfined aquifer acts as the lower boundary condition for the of
365 shallow soil columns assuming pressure and flux continuity at the soil-aquifer interface. The
366 two major assumptions in the GFB approach are: (1) the pressure profile can be linearly
367 interpolated from the aquifer to the first computation node at the bottom of the soil column;
368 and (2) the variability of saturated depth is negligible compared to its absolute value. Three
369 model configurations, (i.e., namely FULL, GFB, and FD) are compared to evaluate the
370 proposed approach and the impact of the assumptions using two synthetic experiments
371 focusing on groundwater recharge (infiltration experiment) and contribution from
372 groundwater to discharge (tilted-v experiment), respectively. The FULL configuration
373 represents a detailed three-dimensional physics-based hydrological model with deep soil
374 columns. In FD, a gravity drainage boundary condition is applied below shallow soil columns
375 mimicking the classical large-scale land surface modelling approach that neglects
376 groundwater dynamics. In contrast, the GFB configuration prescribes our proposed boundary
377 condition below shallow soil columns representing simplified groundwater dynamics
378 compared to FULL.

379 From the results of the infiltration experiment, it is evident that GFB performs considerably
380 better in simulating soil water movement compared to FD, which is consistent across all soil

381 textural classes. The best performance of the GFB configuration relative to FULL is observed
382 across fine-textured soils (e.g., clay). For coarse-textured soils (e.g., sand), however, the
383 differences between FULL and GFB increased as a result of the assumptions introduced in
384 GFB. For the tilted-v experiment, runoff is generated solely due to the convergence of
385 groundwater along the central channel (i.e., no rainfall is applied). At the outlet of the
386 catchment, the cumulative discharge volumes from the FULL and GFB agree well. Our
387 results also demonstrate that the GFB configuration can reproduce the spatial variability of
388 the flow depth well when compared to FULL. The advantage of using GFB is highlighted in
389 this synthetic case by a much lower computing time compared to the FULL configuration.
390 Our model evaluation suggests that GFB can potentially be used to represent groundwater
391 dynamics in large-scale hydrological and land surface modelling applications, especially
392 given its computational efficiency while resulting in relatively minimal loss of performance
393 when compared to a more detailed and integrated hydrological model. It is, however,
394 important to emphasize that our study focuses only on the evaluation of the proposed
395 approach using two synthetic test cases, which consider, for instance, homogeneous soils,
396 simplified topographic slopes, and uniform atmospheric forcing. The GFB approach certainly
397 requires additional corroboration considering real-world and larger model domains studies,
398 including heterogeneity in relief, soil information, and atmospheric forcing.

399

400

401

402

403

404 **Acknowledgements**

405 We gratefully acknowledge the support by the “A MUlti-scale Soil moisture
406 Evapotranspiration Dynamics study” (AMUSED) [grant number NE/M003086/1] and the
407 “Brazilian Experimental datasets for MUlti-Scale interactions in the critical zone under
408 Extreme Drought” (BEMUSED) [grant number NE/R004897/1], both projects funded by
409 Natural Environment Research Council (NERC). Partial support from the NERC “Managing
410 the Risks, Impacts and Uncertainties of drought and water Scarcity” (MaRIUS) project [grant
411 number NE/L010399/1] received by Thorsten Wagener is appreciated and gratefully
412 acknowledged. We would also like to acknowledge the partial support by the Queens School
413 Pump-Priming grant 2016 (University of Bristol). We also appreciate the comments and
414 suggestions from the three anonymous reviewers and the editor, which all helped to improve
415 the quality of this manuscript.

416

417

418

419

420

421

422

423

424

425 **References**

- 426 Abbott, M. B., J. C. Bathurst, J. A. Cunge, P. E. O’Connell, and J. Rasmussen (1986), An
427 introduction to the European Hydrological System — Systeme Hydrologique Europeen,
428 “SHE”, 1: History and philosophy of a physically-based, distributed modelling system, J.
429 Hydrol., 87, 45-59, doi:10.1016/0022-1694(86)90114-9.
- 430 Archfield, S. A., M. Clark, B. Arheimer, L. E. Hay, H. McMillan, J. E. Kiang, J. Seibert, K.
431 Hakala, A. Bock, T. Wagener, W. H. Farmer, V. andréassian, S. Attinger, A. Viglione, R.
432 Knight, S. Markstrom, and T. Over (2015), Accelerating advance sin continental domain
433 hydrologic modeling, Water. Resour. Res., 51, 10078-10091, doi:10.1002/2015WR017498.
- 434 Arnell, N. W. (1999), A simple water balance model for the simulation of streamflow over a
435 large geographic domain, J. Hydrol., 217, 314-335.
- 436 Ashby, S. F., and R. D. Falgout (1996), A parallel multigrid preconditioned conjugate
437 gradient algorithm for groundwater flow simulations, Nucl. Sci. Eng., 124(1), 145– 159.
- 438 Assouline, S., D. Tessier, and A. Bruand (1998), A conceptual model of the water retention
439 curve, Water Resour. Res., 34(2), 223-231.
- 440 Beven, K. J. and H. L. Cloke (2012), Comment on: Hyperresolution global land surface
441 modeling: Meeting a grand challenge for monitoring Earth's terrestrial water by Eric F Wood
442 et al. Water Resources Research, 48 (1). W01801. ISSN 00431397 doi:
443 <https://doi.org/10.1029/2011WR010982>.
- 444 Bierkens, M. F. P. (2015), Global hydrology 2015: State, trends, and directions, Water
445 Resour. Res., 51, 4923-4947, doi:10.1002/2015WR017173.

446 Chen, X., and Q. Hu (2004), Groundwater influences on soil moisture and surface
447 evaporation, *J. Hydrol.*, 297, 285-300.

448 Clark, M. P., Y. Fan, D. M. Lawrence, J. C. Adam, D. Bolster, D. J. Gochis, R. P. Hooper,
449 M. Kumar, L. R. Leung, D. S. Mackay, R. M. Maxwell, C. Shen, S. C. Swenson, and X. Zeng
450 (2015), Improving the representation of hydrologic processes in Earth System Models, *Water*
451 *Resour. Res.*, 51, 5929– 5956, doi:10.1002/2015WR017096.

452 Döll, P., F. Kaspar, and B. Lehner (2003), A global hydrological model for deriving water
453 availability indicators: Model tuning and validation, *J. Hydrol.*, 270(1–2), 105–134,
454 doi:10.1016/S0022-1694(02)00283-4.

455 Famiglietti, J. S., and E. F. Wood (1994), Multiscale modeling of spatially variable water and
456 energy balance processes, *Water Resour. Res.*, 30(11), 3061-3078.

457 Fan, Y., H. Li, and G. Miguez-Macho (2013), Global pattern of groundwater table depth,
458 *Science*, 339(6122), 940-943, doi: 10.1126/science.1229881.

459 Hazenberg, P., Y. Fang, P. Broxton, D. Gochis, G.-Y. Niu, J. D. Pelletier, P. A. Troch, and X.
460 Zeng (2015), A hybrid-3D hillslope hydrological model for use in Earth system models,
461 *Water Resour. Res.*, 51, 8218–8239, doi:10.1002/2014WR016842.

462 Kelleher, C., McGlynn, B. and Wagener, T. (2017), Characterizing and reducing equifinality
463 by constraining a distributed catchment model with regional signatures, local observations,
464 and process understanding. *Hydrol. Earth Syst. Sci.*, 21, 3325–3352, doi.org/10.5194/hess-
465 21-3325-2017.

466 Keune, J., F. Gasper, K. Goergen, A. Hense, P. Shrestha, M. Sulis, and S. Kollet (2016),
467 Studying the influence of groundwater representations on land surface-atmosphere feedbacks
468 during the European heatwave in 2003, *J. Geophys. Res. Atmos.* 121, 13301-13325.

469 Kollet, S. J., and R. M. Maxwell (2006), Integrated surface-groundwater flow modeling: A
470 free-surface overland flow boundary condition in a parallel groundwater flow model, *Adv.*
471 *Water Resour.*, 29(7), 945– 958.

472 Kollet, S. J., and R. M. Maxwell (2008), Capturing the influence of groundwater dynamics on
473 land surface processes using an integrated, distributed watershed model, *Water Resour. Res.*,
474 44, W02402, doi:10.1029/2007WR006004.

475 Kollet, S., M. Sulis, R. M. Maxwell, C. Paniconi, M. Putti, G. Bertoldi, E. T. Coon, E.
476 Cordano, S. Endrizzi, E. Kikinzon, E. Mouche, C. Mügler, Y.-j. Park, J. C. Refsgaard, S.
477 Stisen, and E. Sudicky (2017), The integrated hydrologic model intercomparison project, IH-
478 MIP2: A second set of benchmark results to diagnose integrated hydrology and feedbacks,
479 *Water Resour. Res.*, 53, 867-890, doi:10.1002/2016WR019191.

480 Koster, R. D., M. J. Suarez, A. Ducharne, M. Stieglitz, and P. Kumar (2000), A catchment-
481 based approach to modeling land surface processes in a general circulation model 1. Model
482 structure, *J. Geophys. Res.*, 105(D20), 24,809-24,822.

483 Lam, A., D. Karssenber, B. J. J. M. van den Hurk, and M. F. P. Bierkens (2011), Spatial and
484 temporal connections in groundwater contribution to evaporation, *Hydrol. Earth Syst. Sci.*,
485 15, 2621–2630.

486 Maxwell, R. M. (2013), A terrain-following grid transform and preconditioner for parallel,
487 large-scale integrated hydrologic modeling, *Adv. Water Resour.*, 53, 109-117.

488 Maxwell, R. M. and L. E. Condon (2016), Connections between groundwater flow and
489 transpiration partitioning. *Science*, 353:6297, 377-380, doi:10.1126/science.aaf7891.

490 Meenal, M., and T. I. Eldho (2011), Simulation of groundwater flow in unconfined aquifer
491 using meshfree point collocation method, *Eng. Anal. Bound. Elem.*, 35, 700-707,
492 doi:10.1016/j.enganabound.2010.12.003.

493 Miller, M. P., S. G. Buto, D. D. Susong, and C. A. Rumsey (2016), The importance of base
494 flow in sustaining surface water flow in the Upper Colorado River Basin, *Water Resour. Res.*,
495 52, 3547–3562, doi:10.1002/2015WR017963.Niu, G.-Y., Z.-L. Yang, K. E. Mitchell, F. Chen,
496 M. B. Ek, M. Barlage, A. Kumar, K. Manning, D. Niyogi, E. Rosero, M. Tewari, and Y. Xia
497 (2011), The community Noah land surface model with multiparameterization options (Noah-
498 MP): 1. Model description and evaluation with local-scale measurements, *J. Geophys. Res.*,
499 116, D12109, doi:10.1029/2010JD015139.

500 Oleson, K. W., et al. (2013), Technical description of version 4.5 of the Community Land
501 Model (CLM), National Center for Atmospheric Research, Boulder, Colo.

502 Pinder, G. F., and J. D. Bredehoeft (1968), Application of the digital computer for aquifer
503 evaluation, *Water Resour. Res.*, 4, 1069-1093.

504 Pitman, A. J. (2003), The evolution of, and revolution in, land surface schemes designed for
505 climate models, *Int. J. Climatol.*, 23, 479-510, DOI: 10.1002/joc.893.

506 Prickett, T. A., and C. G. Lonquist (1971), Selected Digital Computer Techniques for
507 Groundwater Resource Evaluation. Illinois State Water Survey, Urbana, Bulletin 55, 3-5.

508 Qu, Y., and C. Duffy (2007), A semidiscrete finite volume formulation for multiprocess
509 watershed simulation, *Water Resour. Res.*, 43, W08419, doi:10.1029/2006WR005752, 2007.

510 Rahman, M., M. Sulis, and S. J. Kollet (2014), The concept of dual-boundary forcing in land
511 surface-subsurface interactions of the terrestrial hydrologic and energy cycles, *Water Resour.*
512 *Res.*, 50, 8531-8548, doi:10.1002/2014WR015738.

513 Richards, L. A. (1931), Capillary conduction of liquids through porous mediums, *Physics*, 1,
514 318.

515 Shen, C., and M. S. Phanikumar (2010), A process-based, distributed hydrologic model based
516 on a large-scale method for surface–subsurface coupling, *Adv. Watr Resour.*, 33, 1524-1541,
517 doi:10.1016/j.advwatres.2010.09.002.

518 Smerdon, B. D., C. A. Mendoza, and K. J. Devito (2007), Simulations of fully coupled lake-
519 groundwater exchange in a subhumid climate with an integrated hydrologic model, *Water*
520 *Resour. Res.*, 43, W01416, doi:10.1029/2006WR005137.

521 Soyly, M. E., E. Istanbuluoglu, J. D. Lenters, and T. Wang (2011), Quantifying the impact of
522 groundwater depth on evapotranspiration in a semi-arid grassland region, *Hydrol. Earth Syst.*
523 *Sci.*, 15, 787–806.

524 Sutanudjaja, E. H., R. van Beek, N. Wanders, Y. Wada, J. H. C. Bosmans, N. Drost, R. J. van
525 der Ent, I. E. M. de Graaf, J. M. Hoch, K. de Jong, D. Karssenber, P. López López, S.
526 Peßenteiner, O. Schmitz, M. W. Straatsma, E. Vannamettee, D. Wisser, and M. F. P. Bierkens
527 (2018), PCR-GLOBWB 2: a 5 arcmin global hydrological and water resources model,
528 *Geosci. Model Dev.*, 11, 2429–2453, <https://doi.org/10.5194/gmd-11-2429-2018>.

529 Troch, P. A., C. Paniconi, and E. E. van Loon (2003), Hillslope-storage Boussinesq model for
530 subsurface flow and variable source areas along complex hillslopes: 1. Formulation and
531 characteristic response, *Water Resour. Res.*, 39(11), 1316, doi:10.1029/2002WR001728.

532 Van Genuchten, M. Th. (1980), A closed-form equation for predicting the hydraulic
533 conductivity of unsaturated soils, *Soil Sci. Soc. Am. J.*, 44,892-898.

534 Wood, E. F., D. Lettenmaier, X. Liang, B. Nijssen, and S. W. Wetzel (1997), Hydrological
535 modeling of continental-scale basins, *Annu. Rev. Earth Planet. Sci.*, 25, 279-300.

536 Wood, E. F., J. K. Roundy, T. J. Troy, L. P. H. van Beek, M. F. P. Bierkens, E. Blyth, P.
537 Döll, M. Ek, J. Famiglietti, D. Gochis, N. van de Giesen, P. Houser, P. R. Jaffé, S. Kollet, B.
538 Lehner, D. P. Lettenmaier, C. Peters-Lidard, M. Sivapalan, J. Sheffield, A. Wade, and P.
539 Whitehead (2011), Hyperresolution global land surface modeling: Meeting a grand challenge
540 for monitoring Earth's terrestrial water, *Water Resour. Res.*, 47, W05301,
541 doi:10.1029/2010WR010090.

542 Yeh, P. J.-F, and E. A. B. Eltahir (2005a), Representation of water table dynamics in a land
543 surface scheme. Part I: model development, *J. Climate*, 18, 1861-1880.

544 Yeh, P. J.-F, and E. A. B. Eltahir (2005b), Representation of water table dynamics in a land
545 surface scheme. Part II: subgrid variability, *J. Climate*, 18, 1881-1901.

546 Zeng, Y., Z. Xie, Y. Yu, S. Liu, L. Wang, J. Zou, P. Qin, and B. Jia (2016), Effects of
547 anthropogenic water regulation and groundwater lateral flow on land processes, *J. Adv.
548 Model. Earth Syst.*, 8, 1106–1131, doi:10.1002/2016MS000646.

549

550

551

552

553 **Tables**

554 Table 1. Hydraulic properties for various soil texture classes (sources: *Johnson et al.*, 1967;
555 *Rawls et al.*, 1982; *Schaap and Leij*, 1998; *Saxton and Rawls*, 2006; *Ghanbarian-Alavijeh et*
556 *al.*, 2010).

Index	Texture	K_s (ms⁻¹)	φ (-)	S_y (%)
1	Clay	1.7x10 ⁻⁷	0.459	2
2	Clay loam	9.4x10 ⁻⁷	0.442	4
3	Silty clay	1.1x10 ⁻⁶	0.481	1
4	Silty clay loam	1.2x10 ⁻⁶	0.482	3
5	Sandy clay	1.3x10 ⁻⁶	0.385	7
6	Loam	1.4x10 ⁻⁶	0.399	11
7	Sandy clay loam	1.5x10 ⁻⁶	0.384	10
8	Silt loam	2.1x10 ⁻⁶	0.439	5
9	Sandy loam	4.4x10 ⁻⁶	0.387	12
10	Silt	5.1x10 ⁻⁶	0.489	8
11	Loamy sand	1.2x10 ⁻⁵	0.390	22
12	Sand	5.8x10 ⁻⁵	0.375	25

557

558

559

560

561

562

563

564

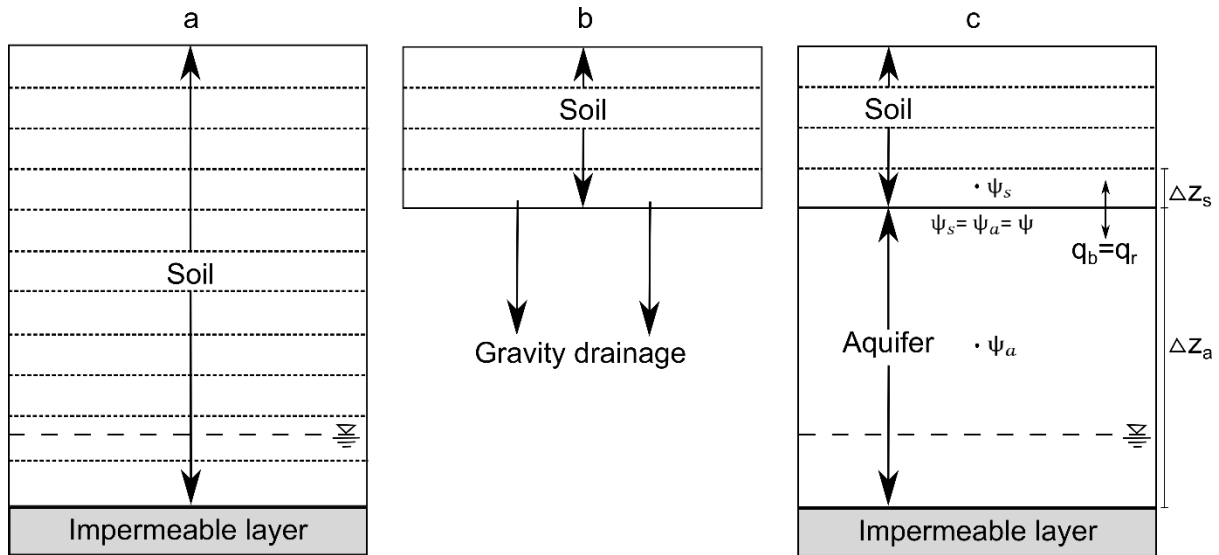
565

566

567

568 **Figures**

569



570

571 Figure 1. Schematic of the vertical extent of (a) a detailed hydrological model, (b) a large-

572 scale model with typically applied free-drainage boundary condition, and (c) the proposed

573 modelling approach of this study (referred as Groundwater Flow Boundary; GFB). While the

574 dotted lines in the figure represent vertical grid discretization, the dashed lines show the

575 location of the groundwater table depth. For clarity, the schematic depicts a column system.

576

577

578

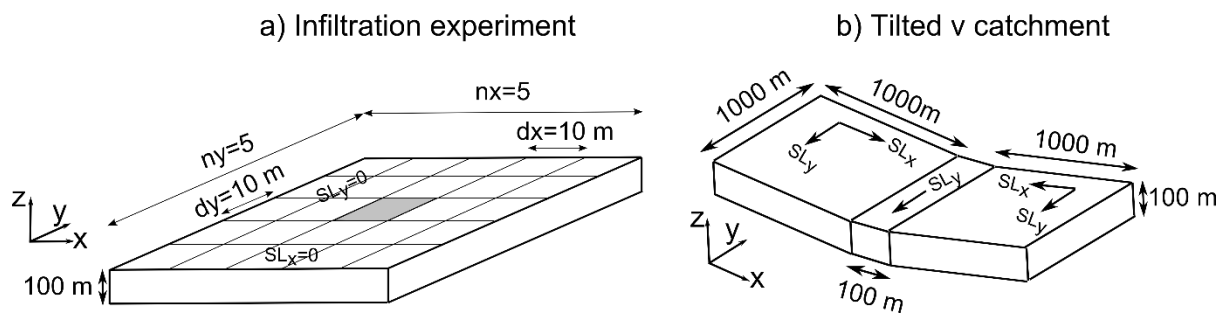
579

580

581

582

583



584

585

586

587

588 Figure 2. Experimental setup for (a) the infiltration experiment and (b) the tilted-v catchment
589 experiment (not to scale). Note that the total subsurface depth is 100 m in both FULL and
590 GFB (10 m soil and 90 m aquifer) configurations. The FD configuration, in contrast,
591 considers a total subsurface depth of 10 m with a gravity drainage lower boundary condition
592 (see Figure 1 for differences in column setup for all cases). Figure 3-6 show results from the
593 central cell of Figure 2a (shown in grey).

594

595

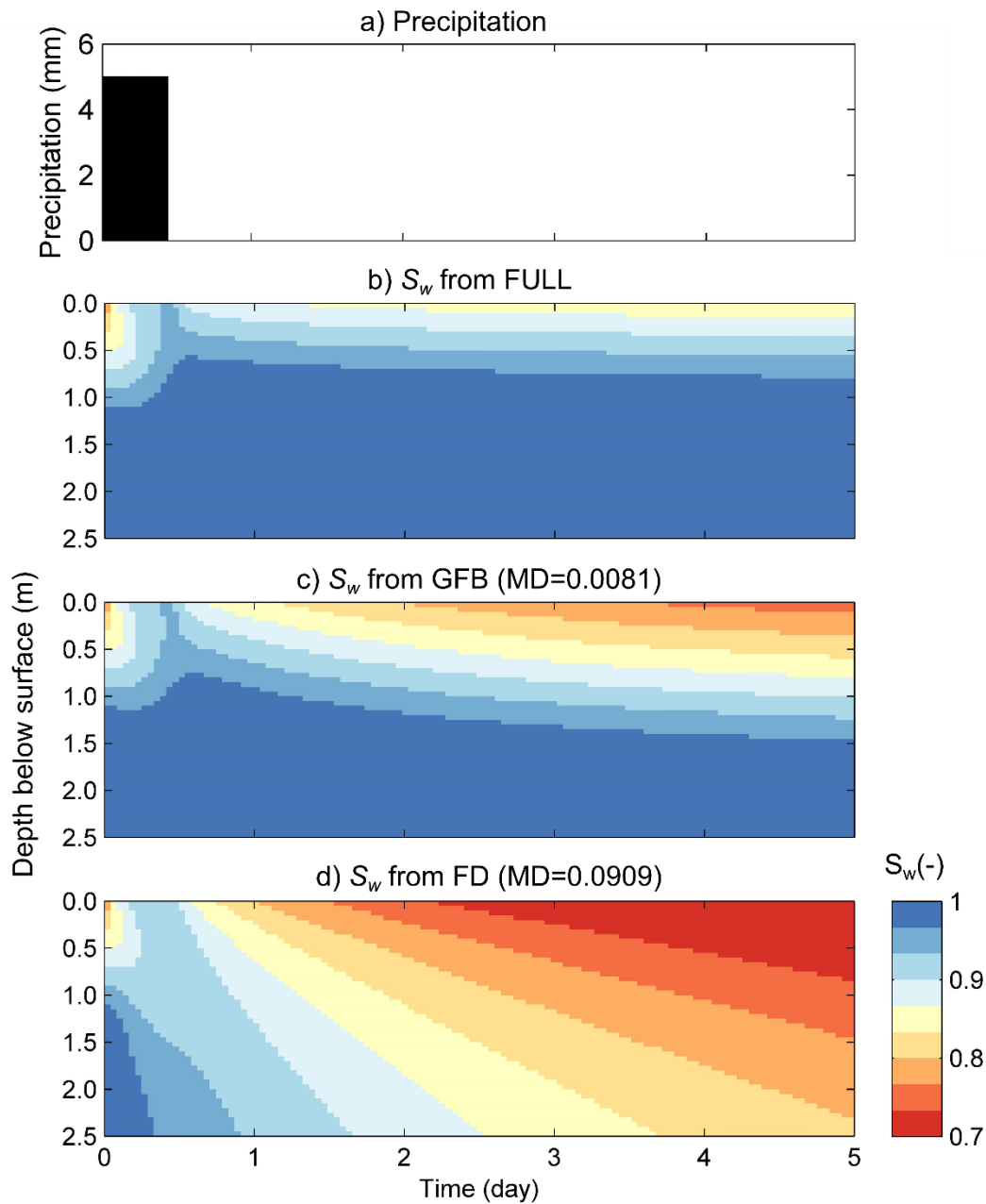
596

597

598

599

600



601

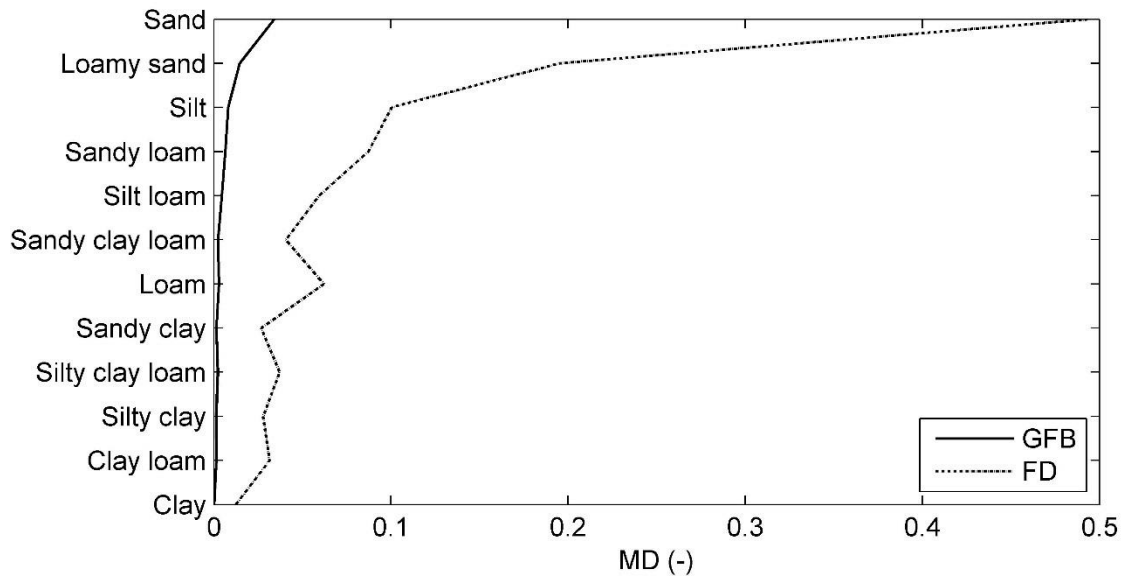
602 Figure 3. (a) Spatially uniform hourly precipitation applied in the infiltration experiment;
 603 hourly relative soil moisture (S_w) profiles from (b) FULL, (c) GFB, and (d) FD model
 604 configurations from the infiltration experiment assuming properties from silty soils. Note the
 605 Mean Difference (MD) of GFB and FD profiles compared to FULL in the respective figure
 606 titles.

607

608

609

610



611

612

613 Figure 4. Mean Difference (MD) of GFB and FD simulated S_w profiles compared to FULL

614 for different soil types from the infiltration experiment.

615

616

617

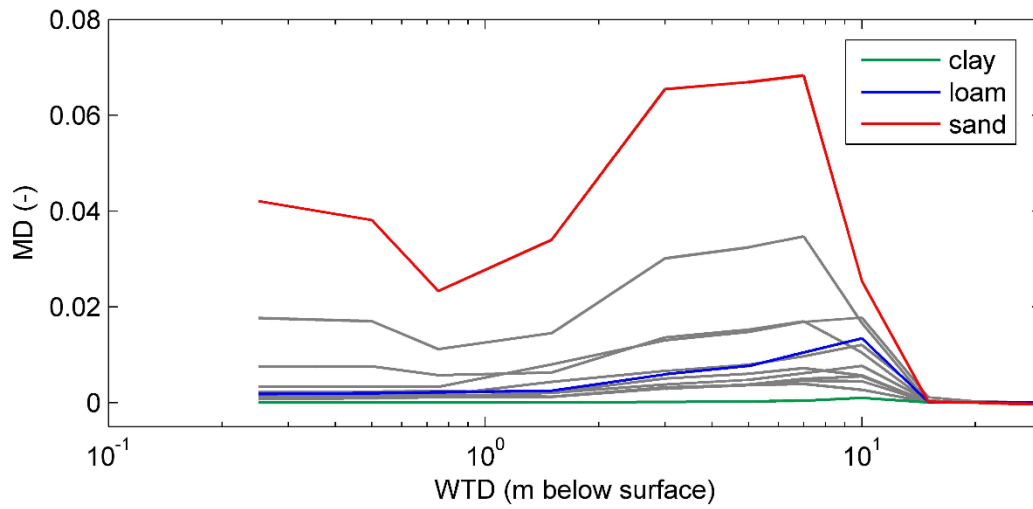
618

619

620

621

622



623

624

625

626 Figure 5. Mean Difference (MD) between FULL and GFB simulated S_w profiles considering
 627 various Water Table Depth (WTD) initializations and soil types for the infiltration
 628 experiment. While sand, loam, and clay are highlighted, results for the other soils are shown
 629 in grey.

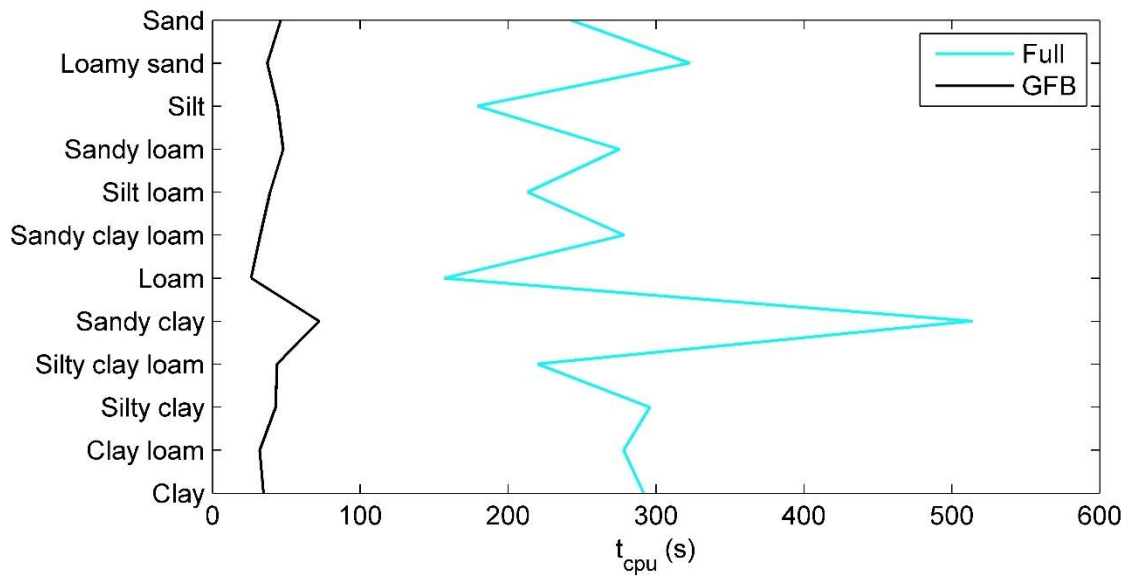
630

631

632

633

634



635

636

637

638

639 Figure 6. Required computing time (t_{cpu}) by the FULL and GFB configurations to simulate

640 the infiltration experiment for different soil textural classes.

641

642

643

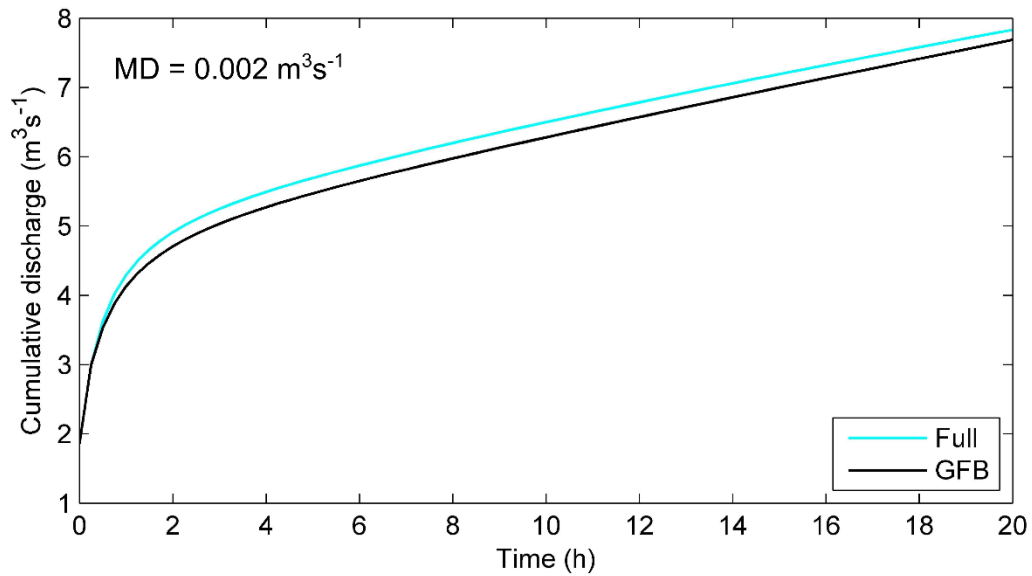
644

645

646

647

648



649

650 Figure 7. Cumulative discharge from the FULL and GFB configurations at the outlet of the
 651 tilted-v catchment. In this simulation, soil hydraulic properties of loam, $SL_x = 0.005$, and SL_y
 652 $= 0.002$ are considered. Note the Mean Difference (MD) between the discharge simulated by
 653 the two configurations. No rainfall is applied in the tilted-v catchment experiment.

654

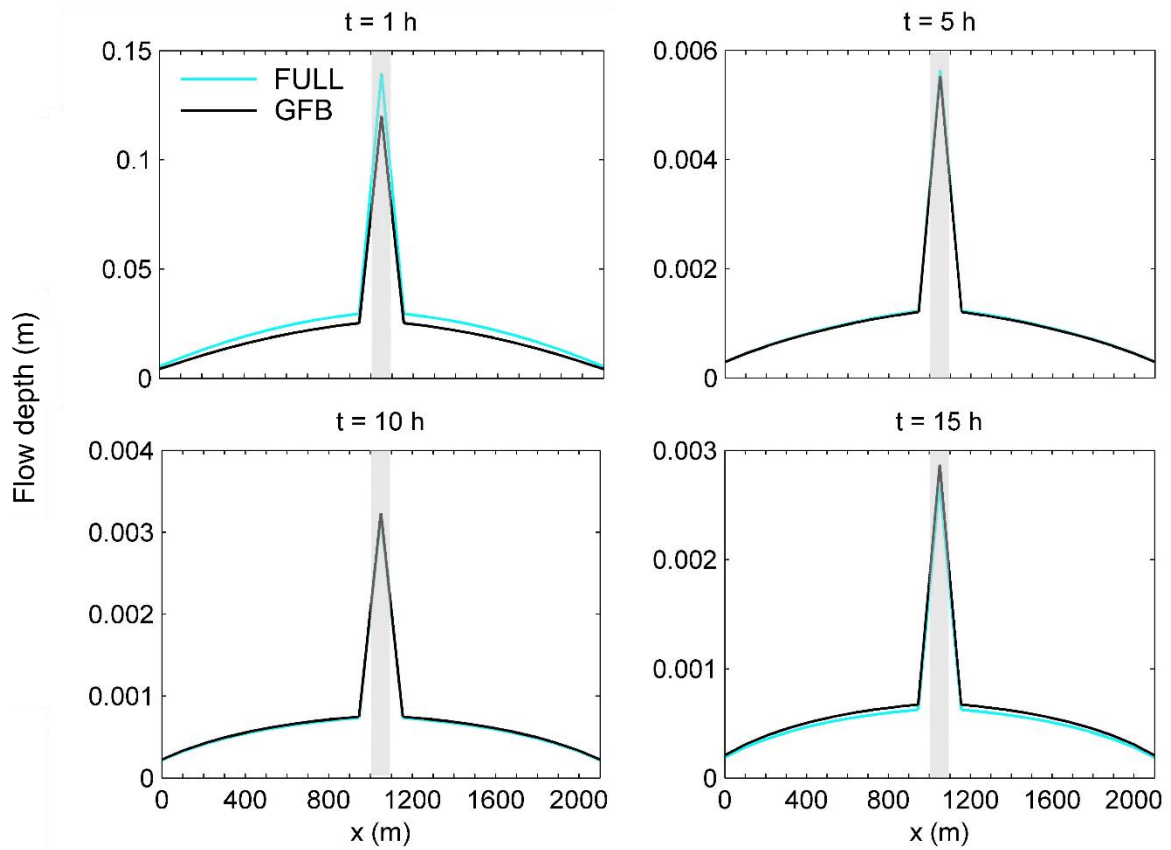
655

656

657

658

659



660

661

662

663 Figure 8. Flow depth along the x -axis at $y = 500$ m of the tilted- v catchment (see Figure 2b)

664 for different simulation time instances. The shaded areas in this figure show the locations of

665 the central channel. Note the different scales for the y -axes.

666

667

668

669

670

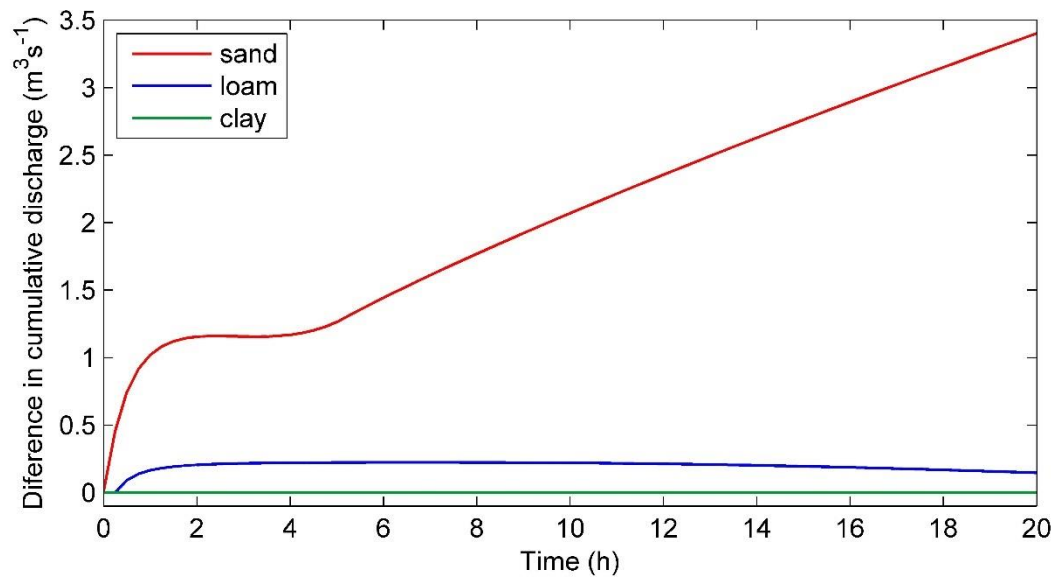
671

672

673

674

675



676

677

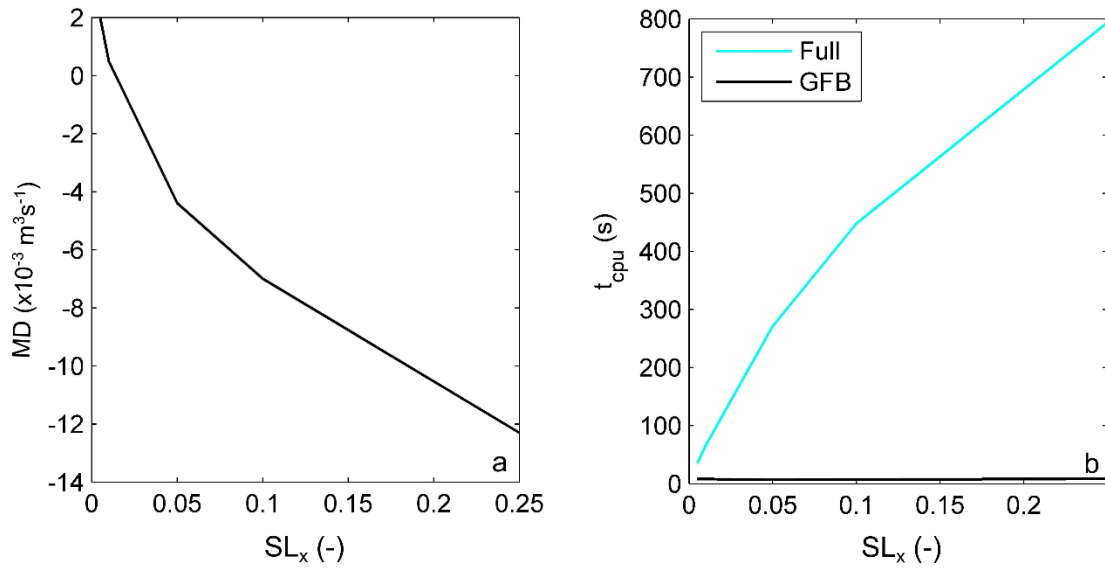
678

679 Figure 9. Differences between cumulative discharge from the FULL and GFB configurations

680 at the outlet of the tilted-v catchment for three soil types. In these simulations, $SL_x = 0.005$

681 and $SL_y = 0.002$ are considered and groundwater table is initially located at the land surface.

682



683

684 Figure 10. (a) Mean Difference (MD) of GFB simulated discharge at the outlet of tilted-v
 685 compared to that of FULL and (b) required computing time (t_{cpu}) by the FULL and GFB
 686 configurations to simulate the tilted-v experiment as a function of topographic slope (SL_x).
 687 Hydraulic properties of loam soil are considered in this simulation.

688

689

690

691